BIOCHEMISTRY

Ketohexokinase-mediated fructose metabolism is lost in hepatocellular carcinoma and can be leveraged for metabolic imaging

Sui Seng Tee[1,2]†, Nathaniel Kim[1,2]‡, Quinlan Cullen[1,2,3]‡, Roozbeh Eskandari[1,2]‡, Arsen Mamakhanyan[1,2], Rami M. Srouji[4], Rachel Chirayil[1,2], Sangmoo Jeong[1,2], Mojdeh Shakiba[5], Edward R. Kastenhuber[6], Shuibing Chen[3,7], Carlie Sigel[7], Scott W. Lowe[6], William R. Jarnagin[4], Craig B. Thompson[6], Andrea Schietinger[5], Kayvan R. Keshari[1,2,3]*

The ability to break down fructose is dependent on ketohexokinase (KHK) that phosphorylates fructose to fructose-1-phosphate (F1P). We show that KHK expression is tightly controlled and limited to a small number of organs and is down-regulated in liver and intestinal cancer cells. Loss of fructose metabolism is also apparent in hepatocellular adenoma and carcinoma (HCC) patient samples. KHK overexpression in liver cancer cells results in decreased fructose flux through glycolysis. We then developed a strategy to detect this metabolic switch in vivo using hyperpolarized magnetic resonance spectroscopy. Uniformly deuterating [2-^{13}C]-fructose and dissolving in D_2O increased its spin-lattice relaxation time (T_1) fivefold, enabling detection of F1P and its loss in models of HCC. In summary, we posit that in the liver, fructolysis to F1P is lost in the development of cancer and can be used as a biomarker of tissue function in the clinic using metabolic imaging.

INTRODUCTION

Carbohydrate metabolism is central to the production of biosynthetic intermediates as well as energy in the form of adenosine triphosphate (ATP). Dietary carbohydrates are broken down into monosaccharides such as galactose, glucose, and fructose (*1*). ATP is used to phosphorylate these hexoses, predominantly catalyzed by hexokinase (HK; E.C. 2.7.1.1). Higher eukaryotes have HKs with little substrate specificity, although lower prokaryotes display a greater repertoire of enzymes that are more selective for particular sugars (*2*). While glucose is the preferred hexose in most cells, fructose metabolism occurs through a specialized pathway, driven by uptake and involving the enzyme ketohexokinase (KHK; E.C. 2.7.1.3).

The liver has long been known to phosphorylate fructose to form fructose-1-phosphate (F1P), in contrast to HKs from other tissues that produce the corresponding 6-phosphate at a significantly slower rate. We now know that this reaction, which generates high concentrations of F1P, is catalyzed by KHK (*3*). Fructose metabolism via KHK is enabled by the expression of cell surface transporters that allow fructose uptake, including members of the facilitative glucose transporters (GLUTs), which consists of 14 members. In the liver, GLUT2 is the predominant transporter for fructose, allowing bidirectional transport with low affinity. GLUT5 is the only transporter specific for fructose, with no ability to transport glucose or galactose, and is expressed mostly in the intestines and sperm (*4*). F1P is further metabolized by aldolase B (Aldo-B) that catalyzes the specific and reversible cleavage of hexoses. While there are three distinct aldolase isozymes, Aldo-B predominates in the liver, kidney, and intestines and preferably cleaves F1P to form glyceraldehyde and dihydroxyacetone phosphate (*5*).

The molecular mechanisms that govern the expression of KHK remain unclear. The human *KHK* gene spans nine exons on chromosome 2p, with two exons (3a and 3c) mutually exclusively spliced to form two isoforms, KHK-A and KHK-C (*6*). KHK-C is responsible for F1P production at physiological fructose concentrations, while KHK-A has been recently reported to be a protein kinase (*7*). There has only been one report of KHK transcriptional control, with the carbohydrate response element binding protein, up-regulating the enzyme in a uric acid–dependent manner (*8*).

Expression of KHK during dysfunction has also been poorly studied. As the ability to break down fructose via KHK is postulated to be a sign of excess, it is likely that loss of this enzyme is associated with disease. There has been a single study that observed lower RNA and reduced KHK enzymatic activity in human clear cell renal cell carcinoma (*9*). More recently, an isoform switch from KHK-C to KHK-A in hepatocellular carcinoma (HCC) has been demonstrated. The authors suggest a c-myc–mediated aberrant splicing mechanism, reducing fructose metabolism in HCC compared to the normal liver (*7*). An integrative genomic characterization of HCC by the Cancer Genome Atlas Research Network [The Cancer Genome Atlas (TCGA)] found that 44% of HCC displayed alteration in the WNT signaling axis (*10*), which includes c-myc as a component. This leaves a majority of HCC cases unaccounted for in terms of KHK expression and the ability to metabolize fructose. Besides cancer, fructose has been implicated in the development of metabolic syndrome in the Western world (*11*), but the expression of KHK in the etiology of this public health issue remains unknown.

If indeed the ability to break down fructose is lost in dysfunction, then it might be possible to exploit this phenotype as a biomarker for disease. Metabolic imaging using hyperpolarized magnetic

[1]Department of Radiology, Memorial Sloan Kettering Cancer Center, New York, NY, USA. [2]Molecular Pharmacology Program, Memorial Sloan Kettering Cancer Center, New York, NY, USA. [3]Weill Cornell Medical College, New York, NY, USA. [4]Department of Surgery, Memorial Sloan Kettering Cancer Center, New York, NY, USA. [5]Immunology Program, Memorial Sloan Kettering Cancer Center, New York, NY, USA. [6]Cancer Biology and Genetics Program, Memorial Sloan Kettering Cancer Center, New York, NY, USA. [7]Department of Pathology, Memorial Sloan Kettering Cancer Center, New York, NY, USA.
*Corresponding author. Email: rahimikk@mskcc.org
†Present address: Department of Diagnostic Radiology and Nuclear Medicine, University of Maryland School of Medicine, Baltimore, MD, USA.
‡These authors contributed equally this work.

resonance spectroscopy (HP-MRS) has the ability to provide real-time, noninvasive quantification of metabolic flux (*12*). Hyperpolarization enhances polarization of nuclear spins, with the most common method being dissolution dynamic nuclear polarization (dDNP). dDNP polarizes an MR-visible nuclei in a frozen sample, with microwave irradiation used to transfer polarization from an organic free radical. Rapid dissolution by injection of a heated physiological buffer enables injection of polarized nuclei into biological systems (*13*). Clinical trials in the prostate (*14*), heart (*15*), and brain (*16*) have been completed, detecting flux from injected HP [1-^{13}C] pyruvate to lactate, in a reaction catalyzed by lactate dehydrogenase (LDH). A loss of KHK activity could potentially be quantified by injection of HP fructose in an analogous manner. HP [2-^{13}C]-fructose has already been demonstrated to be detectable in a mouse model of cancer, with the 6-phosphate form being produced, catalyzed by tumor HK (*17*). In this study, we investigate the expression of KHK in development and disease, with the aim of using fructose metabolism as a potential early biomarker for dysfunction.

RESULTS

KHK expression is limited spatially and temporally

Although immunohistochemical profiling of KHK expression across tissues has been reported (*18*), we attempted to reproduce published results to compare KHK expression across developmental time as well as across organs. In sections of embryonic mice, we observed no staining at embryonic day 9 (E9) and minimal staining at E14. In contrast, E16 sections have developed distinctive livers that contain KHK-positive cells (Fig. 1A). This is in agreement with previous studies (*19*) suggesting that KHK is not synthesized in substantial amounts in the liver until after birth. In addition, this also matches the timeline of mouse liver development, where the liver diverticulum forms by E9 from endodermal layers and hepatoblast differentiation into hepatocyte and biliary cells occurs after E15 (*20*). Further expression of KHK is observed in the adult mouse kidney and intestine as expected (fig. S1A). In adult human tissues, the liver, intestines, and kidney demonstrated strong staining as expected, while the bladder, spleen, and brain were negative (Fig. 1B). Human intestinal organoids derived from human embryonic stem cells (*21*) also

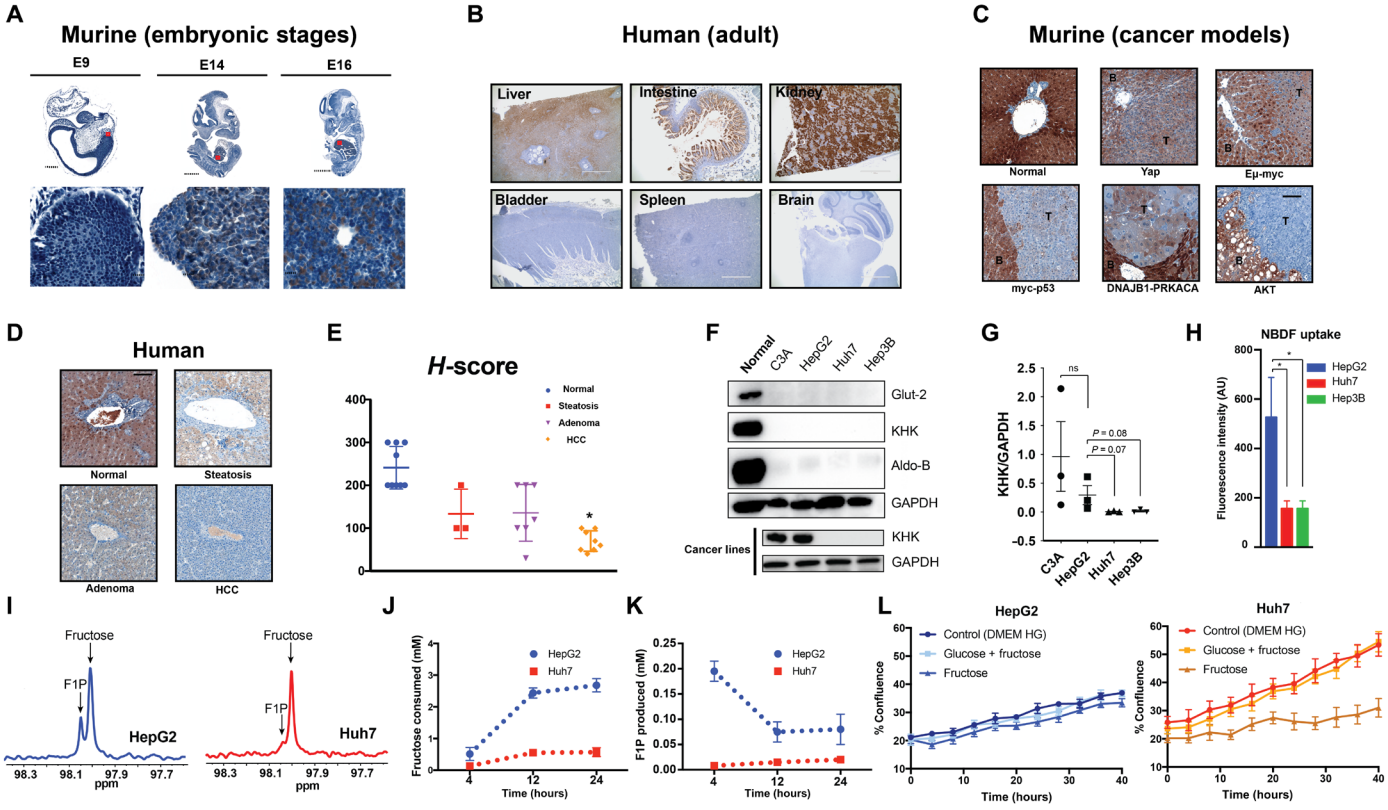

Fig. 1. KHK expression is limited spatially and temporally and lost in cancer. (**A**) Immunohistochemistry (IHC) of embryonic mouse tissue demonstrates lack of expression on E9 with positive staining evident from E14 across to E16. (**B**) Adult human tissues demonstrate staining in the liver, intestines, and kidney with no staining in other tissues. (**C**) Murine liver sections of normal BL6 and models of liver cancer. T represents tumor, while B represents regions of the liver. (**D**) Representative images in normal and diseased liver. Scale bars, 500 μm. (**E**) Semiquantitative scoring of normal liver ($n = 9$) with a mean ± SD value of 241.1 ± 49.6, steatosis ($n = 3$) 133.3 ± 57.5, adenoma ($n = 7$) 135.7 ± 63.3, and HCC ($n = 8$) 70.0 ± 23.9. (**F**) Western blots showing loss of proteins associated with fructose metabolism in cancer compared to normal with associated (**G**) densitometric analysis. ns, not significant; GAPDH, glyceraldehyde phosphate dehydrogenase. (**H**) Cells incubated with 10 μM of the fluorescent fructose analog, 1-NBDF. Fluorescence intensity displayed statistically significant reduction of 1-NBDF uptake in HCC cells compared to HepG2. AU, arbitrary units. (**I**) Representative ^{13}C NMR spectra of cells supplemented with [2-^{13}C]-fructose. Fructose consumption in media (**J**) of HepG2 cells increased over 24 hours, with 2.8 ± 0.9 mM fructose consumed compared to 0.8 ± 0.2 mM in Huh7. F1P levels in HepG2 cells (**K**) peaked 4 hours after labeling at 0.19 ± 0.06 mM while undetectable in Huh7. (**L**) HepG2 cells grown in 25 mM fructose proliferated at similar rates to control, while Huh7 cells were unable to grow at the same rate. All *P* values were calculated using a Student's *t* test with $^*P < 0.05$. DMEMHG, Dulbecco's modified Eagle's medium high glucose.

demonstrated a time-dependent expression of KHK (fig. S1B). Only well-differentiated organoids, approximately 80 days after addition of defined growth factors, expressed KHK.

KHK expression is reduced in mouse models and human liver disease

To assess the role of KHK in disease, we performed immunohistochemistry (IHC) on a number of genetically engineered mouse (GEM) models of liver cancer. In five distinct GEM models with mutations in different oncogenes and/or tumor suppressors, we observed markedly lower levels of KHK expression in tumor regions compared to adjacent normal tissue (Fig. 1C). While the histological appearance of the liver tumors was morphologically distinctly dependent on the mutation present, KHK appeared to be uniformly down-regulated, suggesting that reduction of fructose metabolism may confer a selective advantage in tumorigenesis. To ensure clinical relevance, we then mined publicly available expression databases across different cancer types to query the level of proteins involved in fructose metabolism. In TCGA, across 23 different cancer types, normal samples showed higher expression of KHK compared to paired tumor samples in cholangiocarcinoma, chromophobe renal cell carcinoma, renal papillary cell carcinoma, and, significantly, HCC (fig. S1C). Within the HCC cohort, expression of Glut2, KHK, and Aldo-B trended higher in normal samples, compared to paired tumor samples. This trend is statistically significant in the molecular subtype, iCluster-1, that has been previously shown to have worse prognosis compared to other subtypes, across all proteins involved in fructose metabolism (fig. S1D).

Last, we investigated KHK expression in patient FFPE sections. IHC of normal (n = 9), steatotic liver (n = 3), adenoma (n = 7), and HCC (n = 8) sections probed using a KHK antibody showed reduced enzyme expression in disease as shown in Fig. 1D. The slides were reviewed by a pathologist (C.S.) and were assigned semi-quantitative scores based on a combined, multiparametric H-score (*22*) (Fig. 1E). Normal liver tissue displayed a mean score of 241.1 ± 49.6. Steatotic and adenoma samples displayed lower H-score values but were not statistically significant compared to normal (133.3 ± 57.5 and 135.7 ± 63.3, respectively). However, human HCC samples consistently presented the lowest H-scores with a mean of 70.0 ± 23.9, which was statistically significant compared to normal human liver tissue.

KHK expression is lost in HCC and results in reduced fructose derived F1P

As KHK expression appeared to be tightly controlled in development and down-regulated in cancer models as well as humans, we investigated whether this enzyme in cancer cell lines in comparison to normal human hepatocytes. Whole cell lysates were blotted for KHK, as well as associated transporters and Aldo-B. While normal lysates from primary hepatocytes demonstrated strong expression of proteins associated with fructose metabolism at the transporter and enzyme levels, we found that the liver cancer cell lines displayed much reduced expression of the transporter as well as KHK and Aldo-B (Fig. 1F). It was challenging to Western blot these cell lines in the same gel with normal hepatocytes, given the dynamic range of protein levels, so the Western blots were repeated for the cell lines. The human hepatoblastoma cell line HepG2 and a derivative HepG2/C3A express the highest levels of the KHK as compared to the HCC cell lines Huh7 and Hep3B (Fig. 1G). This trend was also observed across a range of intestinal cancer cell lines when compared to normal intestinal lysates (fig. S1E).

To characterize total fructose uptake, we investigated whether HCC cell lines were able to uptake the fluorescent fructose derivative, 1-(7-nitro-1,2,3-benzadiazole)-fructose (1-NBDF). Accordingly, HepG2 cells retain the highest levels of fluorescent 1-NBDF compared to HCC cells (Fig. 1H and fig. S1F). To confirm that KHK-mediated metabolism was indeed lost in HCC cells, we incubated cells with [2-^{13}C]-fructose. Using ^{13}C NMR, we were able to identify that [2-^{13}C]F1P (fructose-1-phosphate) exhibited characteristic splitting due to J-coupling between the ^{13}C2 and ^{31}P, providing a means of quantifying F1P via the downfield resonance (Fig. 1I and fig. S1G). While both HepG2 and Huh7 displayed an increase of fructose consumption over time, HepG2 consumed over twice the amount of fructose after 24 hours compared to Huh7 cells (Fig. 1J). Accordingly, higher levels of [2-^{13}C]F1P were measurable in HepG2 lysates as early as 4 hours after [2-^{13}C] incubation, while F1P was nearly undetectable in Huh7 cells (Fig. 1K). We further confirmed that this resonance was indeed F1P by incubating HepG2 cells with a selective KHK inhibitor (fig. S1H). Furthermore, these hepatoblastoma cells are also able to proliferate in fructose as the sole carbon source, while Huh7 cells were not able to grow in fructose alone at the same rate (Fig. 1L). These results suggest that the ability to break down fructose is tightly controlled over developmental time and spatially across different organs with loss KHK-mediated fructose metabolism in disease.

Overexpression of KHK reroutes metabolism and results in cell death

With this metabolic switch, we sought to characterize the long-term effects of KHK overexpression. First, we transiently overexpressed KHK fused to green fluorescent protein (GFP) in both Huh7 and Hep3B cells (fig. S2A). Incubation of these cells with fructose for 6 days results in near-complete cell death for GFP-positive cells (Fig. 2B). To more deeply study the metabolic consequences of KHK overexpression, we developed stable KHK-overexpressed (KHK-OV) HepG2 and Huh7 cells (Fig. 2C). Tracing with [2-^{13}C]-fructose in these cell lines reveals a marked increase in [2-^{13}C]-fructose-1-phosphate as expected (Fig. 2, D and E). To establish the effect of KHK overexpression downstream of F1P, cells were incubated with [U-^{13}C] fructose, and stable isotope tracing into glycolysis was measured using liquid chromatography–mass spectrometry (LC-MS) (Fig. 2F) following 4 hours of incubation. Furthermore, both cell lines demonstrated reduced generation of labeled lactate as well as citrate-derived fructose as compared to the glucose condition, highlighting the reduction in carbon flux both into glycolysis and subsequent metabolism into the tricarboxylic acid (TCA) cycle (Fig. 2G and fig. S2A). KHK-OV–expressed Huh7 cells demonstrated a reduction in the total pool of ATP as well as the resulting adenosine monophosphate (AMP)/ATP ratio (Fig. 2, H to J), in line with the enzymatic action of KHK. While KHK-OV Huh7 cells show a characteristic decrease in all the components of glycolysis, KHK-OV HepG2 cells gain the capacity to perform gluconeogenesis from fructose, highlighted by the formation of m + 3 glucose-6-phosphate and m + 3 glucose (Fig. 2G and fig. S2A). This is in line with the canonical connection between KHK expression and gluconeogenesis, suggesting that in the presence of fructose, KHK reverses the net direction of glycolytic flux. Together, these data support the notion that HCC cells are unable to survive in the presence of fructose when KHK expressed, rerouting

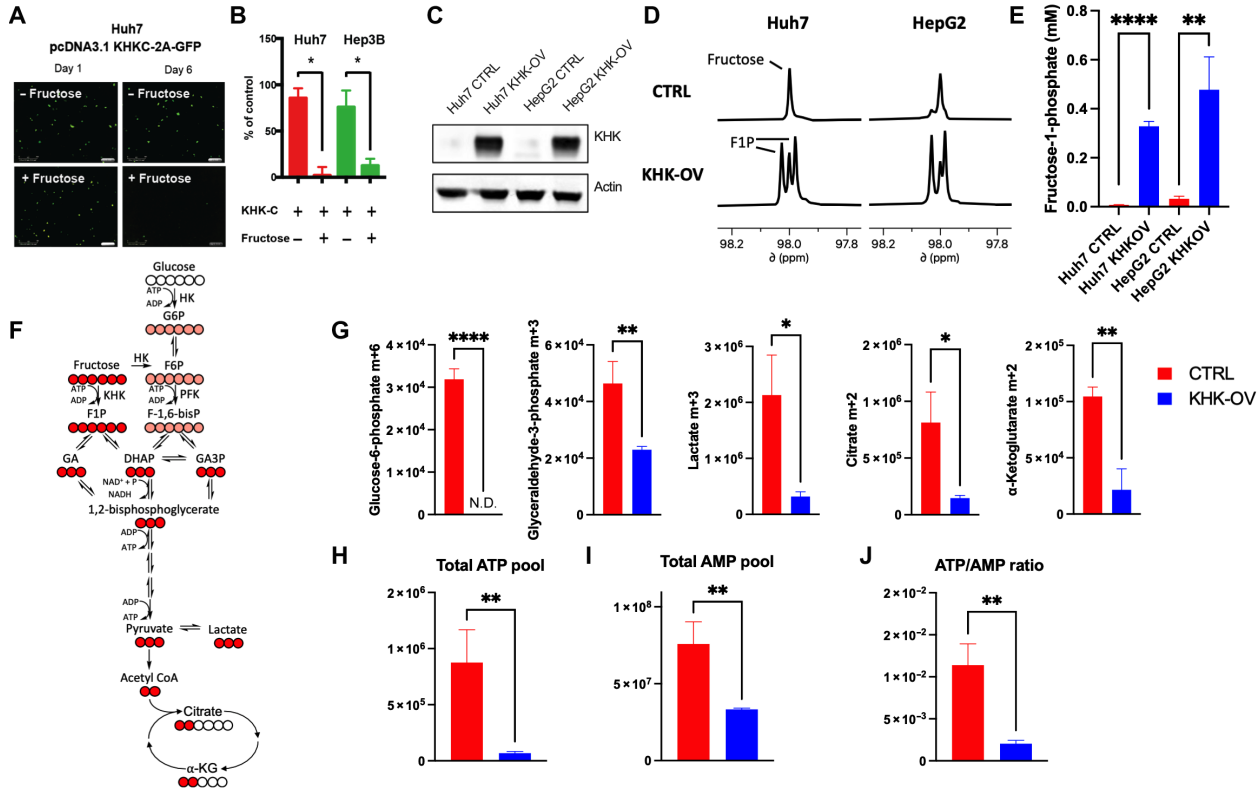

Fig. 2. KHK overexpression shunts ^{13}C fructose through F1P and reduced glycolysis. (**A**) Fluorescent micrographs of Huh7 cells transiently transfected with plasmid expression KHKC-2A-GFP. A progressive loss of fluorescent cells was observed in the presence of DMEM supplemented with 12.5 mM fructose, indicating negative selection of HCC cells that express KHK. (**B**) Similar results were quantified with transfected Hep3B cells, with only 12.5 ± 1.2% fluorescent cells remaining after 6 days of culture in the presence of fructose ($n = 3$ biological replicates are used per group, and statistics were calculated using a Student's t test with a $^*P < 0.05$). (**C**) Representative Western blot demonstrating increased expression of KHK for stable HepG2 and Huh7 cell lines as compared to control virus. (**D**) Representative ^{13}C NMR data showing increased generation of intracellular [2-^{13}C] fructopyraonse-1-phosphate after incubation with [2-^{13}C]fructose for 4 hours in KHK overexpression cells as compared to control vector. (**E**) Quantitation of ^{13}C F1P generated in 4 hours (means ± SD, $n = 3$ biological replicates). (**F**) Metabolic scheme highlighting the isotope labeling of glycolytic intermediates and the TCA cycle when cells are rapidly exposed to [U-^{13}C]fructose. ADP, adenosine diphosphate; NADH, reduced form of NAD$^+$; DHAP, glyceraldehyde and dihydroxyacetone phosphate; CoA, coenzyme A; GA, glyceraldyhyde; GA3P, glyceraldehyde 3-phosphate; alphaKG, α-Ketoglutaric acid. (**G**) Key enriched intermediates from [U-^{13}C] fructose are reduced with KHK overexpression in Huh7 cells (means ± SD, $n = 3$ biological replicates). N.D., not determined. (**H**) Total ATP and (**I**) AMP pools as well as the (**J**) ATP/AMP ratio are significantly reduced with KHK overexpression in Huh7 cells (means ± SD, $n = 3$ biological replicates). All P values were calculated using a Student's t test with $^*P < 0.05$, $^{**}P < 0.01$, and $^{****}P < 0.0001$.

metabolism and implying that loss of KHK activity and metabolism of fructose are required for cancer cell survival.

Toward metabolic imaging of fructose metabolism in the liver

The ability to noninvasively detect metabolism in real time has resulted in the rapid adoption of HP-MRS in clinical trials. As a proof of concept, HP [2-^{13}C]-fructose has been injected into a transgenic prostate cancer model; however, the T_1 relaxation time, which dictates HP probe lifetime, of [2-^{13}C]-fructose was reported to be 16 s at 11.7 T. Ultimately, this approach was not feasible for the detection of F1P, and to date, there are no viable strategies for measuring this flux noninvasively in vivo.

To this end, we took advantage of recent developments from our laboratory to leverage solvation using D_2O (*23*). In addition, we developed a novel method to deuterate [2-^{13}C]-fructose using a ruthenium-on-activated-carbon (Ru/C) catalyst under a hydrogen atmosphere in D_2O as a deuterium source. This has recently been demonstrated on other sugars such as glucose, ribose, and deoxyribose (*24*). Site selectivity can be achieved by protection of hydroxyl groups as acetals, as H-D exchange does not occur on positions adjacent to protected hydroxyls (Fig. 3A). Figure 3B depicts representative dynamics of [2-^{13}C]-fructose dissolved in H_2O (black trace) or U-^{2}H-[2-^{13}C]-fructose dissolved in D_2O, with the latter displaying a marked extension of the HP signal. Quantification of the T_1 values for [2-^{13}C]-fructose was measured to be 18.9 ± 0.1 s, while [U-^{2}H, 2-^{13}C] fructose showed a marked increase to 92.5 ± 17.2 s (Fig. 3, C and D).

To further this new strategy for HP F1P detection, we used an autochthonous AST model that expresses SV40 large T-antigen driven by albumin-specific Cre recombinase in hepatocytes. Using this optimized approach, we imaged both mice harboring HCC and their aged-matched controls (Fig. 3, E and F). Fructose exists as multiple isomers that can be readily resolved in ^{13}C NMR, the predominant form being the fructopyranose [approximately 70% in solution (*17*)]. Representative spectra demonstrate not only the HP fructopyranose and furanose forms but also that of the HP F1P, which exists predominantly as a pyranose (Fig. 3G). Given that the tumors are ubiquitous throughout the liver, we quantified regions of interest of the

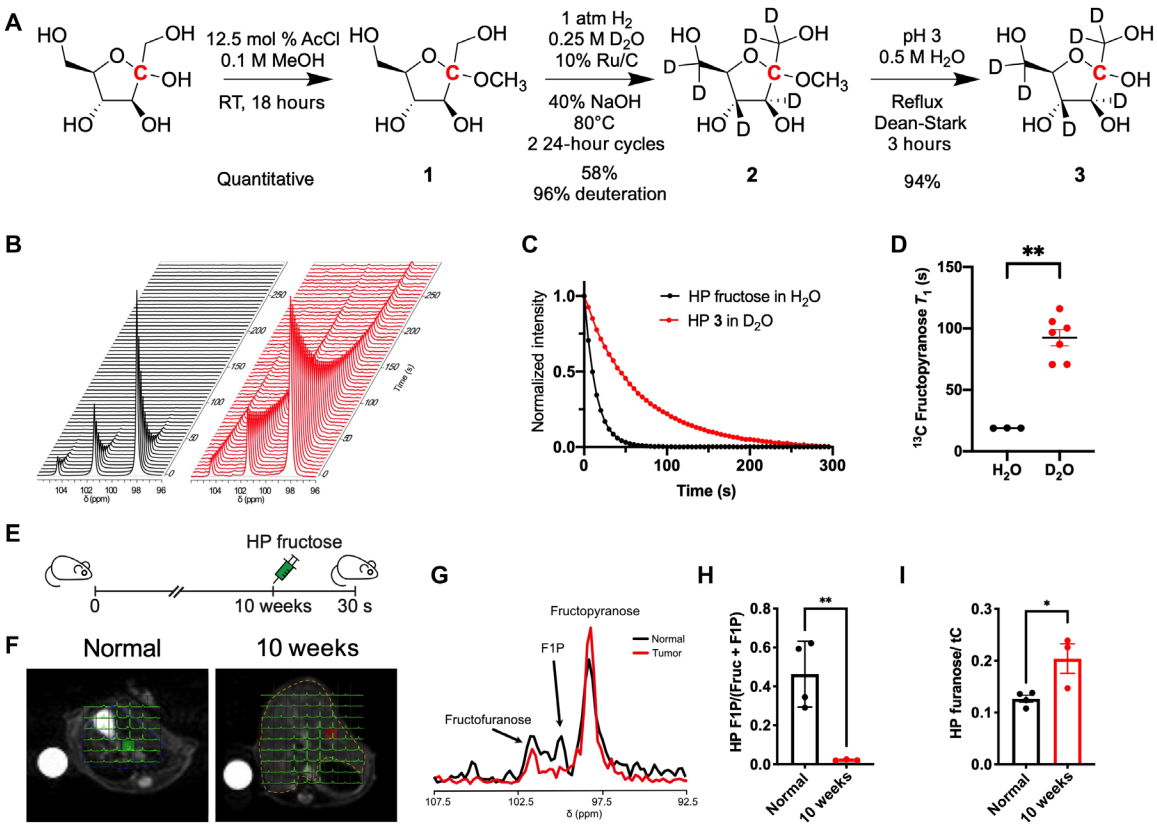

Fig. 3. Metabolic imaging of liver disease using Hyperpolarized [2-^{13}C]fructose. (**A**) Synthesis of deuterated [2-^{13}C]fructose **3**. RT, room temperature. (**B**) Dynamic spectra of HP [2-^{13}C]fructose dissolved in H_2O (black) and HP **3** dissolved in D_2O (red) on a 1-T ^{13}C NMR spectrometer shows prolonged hyperpolarized signal as a result of substrate deuteration and dissolution in D_2O. (**C**) Quantification of T_1 values measured using the area under the curve obtained from dynamic spectra. (**D**) Calculated T_1 values were found to be 18.9 ± 0.1 s for HP [2-^{13}C]fructose dissolved in H_2O and 92.5 ± 17.2 s for HP **3** dissolved in D_2O. (**E**) Schematic of [2-^{13}C]fructose injection in the autochthonous model of liver cancer, at 10 weeks of age. The autochthonous mouse model was imaged using hyperpolarized (HP) [2-^{13}C]fructose MRI at 10 weeks of age against age-matched controls (**F**). (**G**) Healthy livers produce F1P as shown by HP MRI, whereas disease state livers exhibit decreased production of F1P. Typical spectra of healthy and disease state livers obtained from HP MRI infusions showing decreased production of F1P in liver disease. (**H**) The observed ratio of F1P to (fructose + F1P) using HP fructose imaging can be used to diagnosis liver cancer. (**I**) The observed ratio of the HP furanose peak to total carbon signal is significantly increased in liver disease and can be used to diagnosis liver cancer (means ± SD, $n = 4$ normal and $n = 3$ 10-week tumor biological replicates). All P values were calculated using a Student's t test with $^*P < 0.05$ and $^{**}P < 0.01$.

entire lobes of the liver for both normal and tumor mice. Quantification of this resonance demonstrated significantly decreased HP F1P generation in 9- to 10-week-old HCC mice as compared to controls (Fig. 3H). This was additionally confirmed in nude mice, demonstrating similar HP F1P levels to aged matched control AST mice (fig. S3). Furthermore, an increase in the HP furanose peak is observed in HCC mice, highlighting a concomitant decrease in the total pyranose signal, further confirming the metabolism through F1P (Fig. 3I).

Confirmation of metabolic rewiring in liver cancer

To verify that metabolic imaging can detect altered KHK activity, we performed in vivo ^{13}C isotopic tracer experiments. First, we took advantage of a tamoxifen-induced SV40 large T-antigen liver model and assessed KHK expression at 50 days after tamoxifen administration. Analogous to our previous animal models, the KHK expression level was completely lost throughout the liver (fig. S4A). To assess KHK loss in time, using the same AST model that expresses SV40 large T-antigen driven by albumin-specific Cre recombinase in hepatocytes, we measured KHK expression with age (Fig. 4A). This model of liver cancer also displayed substantial loss of KHK expression (Fig. 4, B and C). Measurement of labeled fructose after a rapid intraperitoneal injection showed a significant reduction in plasma-labeled fructose with evolution of the model as well as a significant loss in labeled glucose derived from gluconeogenesis (Fig. 4, D and E). This is consistent with our in vitro KHK-OV data, demonstrating the role of KHK in driving gluconeogenesis. Moreover, at 10 weeks, plasma levels of labeled lactate derived from fructose are increased, suggesting the same rerouting of metabolism observed in our hyperpolarized imaging data (Fig. 4F) and implicated in the KHK-OV in vitro experiments (fig. S2). Tumor levels of labeled F1P are reduced as early as 4 weeks (Fig. 4H), in line with the reduction in F1P generated in the tamoxifen-induced model (fig. S4E), consistent with loss of KHK as a mediator of metabolic flux.

DISCUSSION

KHK is an ancient enzyme with more similarity to prokaryotic HKs that are substrate specific. Persistence of this enzyme is limited to a few organs and provides a selective advantage when nutrient sources

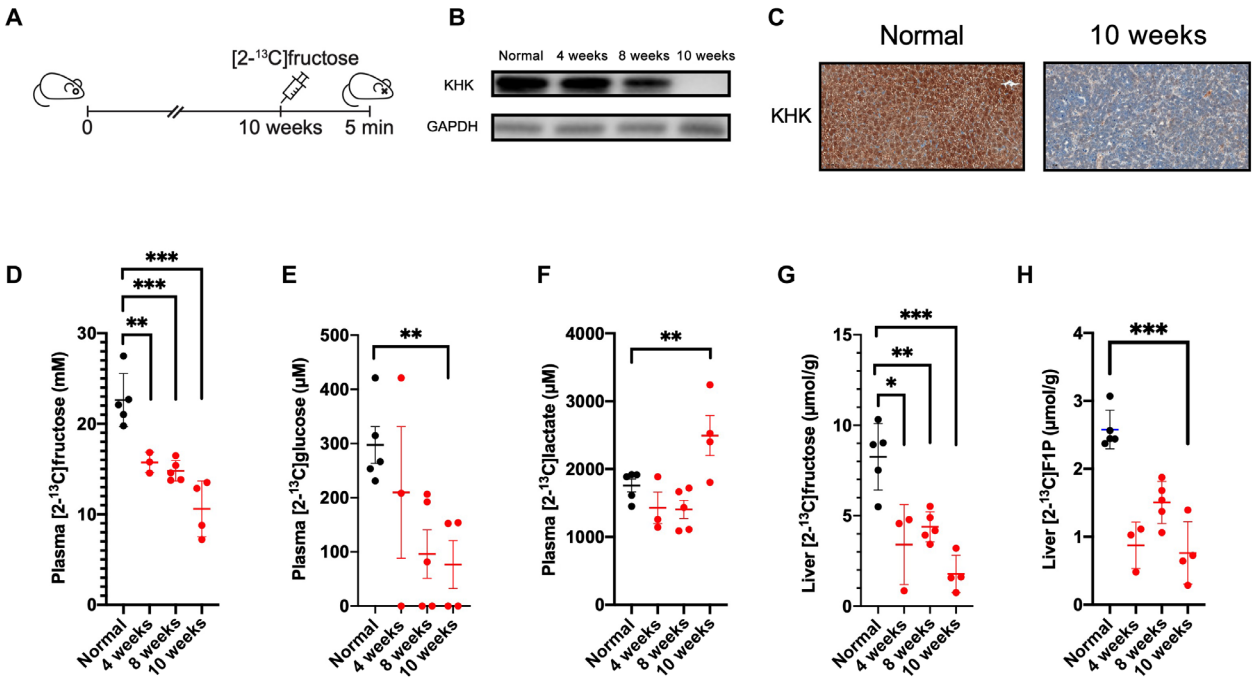

Fig. 4. Isotope tracing of fructose metabolism in liver cancer. (**A**) Scheme of the rapid isotope tracing experiment. (**B**) Western blot analysis showing progress loss of KHK with age. (**C**) Immunohistochemistry confirming loss of KHK when comparing 10-week to age-matched normal. (**D**) Plasma [2-^{13}C]fructose, (**E**) [2-^{13}C]glucose, and (**F**) [2-^{13}C]lactate measured in mice, 5 min after injection of [2-^{13}C]fructose. (**G**) [2-^{13}C]fructose and (**H**) [2-^{13}C]fructose-1-phsophate in the mouse liver per tumor 5 min after injection of [2-^{13}C]fructose (means ± SD, $n = 5$ normal, $n = 3$ 4-week, $n = 5$ 8-week, and $n = 4$ 10-week tumor biological replicates). All P values were calculated using a Student's t test with $^{*}P < 0.05$, $^{**}P < 0.01$, and $^{***}P < 0.001$.

are scarce; whatever little available fructose can be converted to glucose for systemic use. This may explain the presence of this enzyme even in organisms that are mainly carnivorous (*25*)—while there is a trade-off between energy yield and protein cost (*26*), limiting expression to particular tissues might be an efficient way to ensure metabolic flexibility in times of low nutrient availability.

Analysis of KHK sequence homology revealed little similarity to other mammalian HKs with the enzyme more closely related to prokaryotic ribokinases (*6*). It has been postulated that persistence of this ancient enzyme provided a selective advantage to maximize usage of any low, intermittent levels of fructose available in times of need (*27*). This is supported by tracing studies of the fate of ingested fructose in humans, with more than 50% being converted to glucose (*28*), the preferred hexose in most tissue types. Therefore, the ability to break down fructose is a sign of good times, arguing for strict temporal and spatial control of KHK expression according to nutrient availability.

As the presence of KHK function is specialized and its distribution limited, we hypothesized that its expression would be down-regulated in dysfunction. Furthermore, KHK has been posited as a driver of metabolic dysfunction, so homeostatic control and negative feedback mechanisms must exist when fructose metabolism through this pathway results in harmful consequences. In a panel of liver and intestinal cancer cell lines, we observe not only a loss of KHK but also reduced expression in fructose-associated transporters as well as the aldolase (Aldo-B) that is responsible for breaking down F1P. Further strengthening our hypothesis is the observation that human HCC samples appear to down-regulate KHK. Recent work in a genetically modified mouse model of intestinal tumor has shown avid metabolism of fructose via KHK (*29*). The authors hypothesize that high-fructose corn syrup, which consists of glucose:fructose in a 45:55 ratio, results in increased glycolysis and fatty acid synthesis as a result of KHK-dependent ATP depletion. While our results appear contrary to their body of work in mouse models with respect to KHK expression in cancer, it may be attributed to differences in human and mouse physiology, as well as tissue-specific regulation of fructose metabolism.

As the KHK presence may be a clinically relevant, we were motivated to explore the mechanisms that controlled KHK expression. Regulation of KHK expression during development is also unknown, except for the observation that enzymatic activity is low in the fetal liver (*19*), with a switch from KHK-A to KHK-C in the adult (*30*). KHK expression is a late event during development, with several reports noting its absence until after birth. Breast milk contains no fructose, so the extracellular signals that turn on KHK remain a mystery. The same is seen in tissue differentiation—pluripotent cells do not appear to contain KHK until growth factors are present to direct differentiation of specialized cell types. Directed differentiation of mouse intestinal organoids has shed some light on KHK expression in the small intestine, with stem cells seeming to lack the enzyme. When these stem cells are differentiated into absorptive enterocyte and secretory goblet cells, they respond to fructose stimulation by expressing KHK, as measured by real-time polymerase chain reaction (PCR) (*31*). Conservation of this expression pattern in human small intestine remains unknown.

While there have been recent reports where GLUT5-mediated fructose uptake was increased in acute myeloid leukemia (*32*) and

lung cancer (*33*), there has been no evidence that fructose was broken down via KHK. It is entirely possible that this ability to metabolize fructose is mediated by HK. Although HKs have a much lower K_m for glucose, these enzymes have a broad preference for hexoses and are able to phosphorylate fructose in the 6-position.

The ability to detect fructose metabolism has been pursued for over a decade using a multitude of imaging modalities including fluorescence (*34*) and positron emission tomography (*35*). Neither of these modalities has the ability to distinguish KHK- versus HK-mediated fructose metabolism. However, HP-MRS has the ability to differentiate phosphorylation of fructose to either F6P or F1P. While HK-mediated fructose metabolism has previously been implicated using HP [2-^{13}C]-fructose (*17*), this is the first report using an HP probe to directly measure KHK-catalyzed formation of F1P, further confirmed in the same models using extensive isotope tracing within a similar timeframe. While we demonstrate that KHK down-expression in liver tumors appears to be a relatively early event, the magnitude of loss and subsequent sensitivity of detection using molecular imaging remain to be determined. Nevertheless, the ability to noninvasively detect fructose metabolic flux through KHK opens the possibility of early detection of dysfunction in tissues that normally metabolize fructose. This would have a substantial impact in the field of metabolic disease, organ transplantation, infection, toxicity and cancer. It is tempting to suggest that if KHK is wired for metabolic flexibility, then its loss would be an early event present an opportunity for disease detection as quickly as possible to allow rapid intervention. This is further supported by recent reports arguing for the loss of KHK-C in the development of nonalcoholic fatty liver disease and differential use of fructose (*36*, *37*).

In conclusion, we have shown that control of KHK expression is controlled tightly over space and time. Viewed in the context of enabling metabolic flexibility, we demonstrate that in cancer, canonical fructose metabolism is lost, trading off the ability to use a scarce nutrient for rapidly incorporating biomass and ATP using glucose. This loss extended to human liver cancer, suggesting a novel biomarker. Last, we explored the potential of using a previously short-lived metabolic imaging modality and lengthening it significantly for the purpose of translating HP-MRS for detection of fructose metabolism.

METHODS

Cell culture conditions

HepG2, Hep3B, and Huh7 cells were obtained from the American Type Culture Collection and cultured in RPMI 1640 (Gibco) media supplemented with 10% fetal bovine serum and 2.5 mM L-glutamine, unless indicated otherwise. All cells were grown under standard culture conditions, incubated at 37°C in 5% CO_2. For mitogen-activated protein kinase kinase inhibition studies, U0126 was obtained from Cayman Chemicals and used at 100 nM. For transfection studies, KHK-C (NM_006488) tagged with GFP on the C terminus was constructed and purchased from Origene (Rockville, MD) and transfected using the jetPRIME transfection reagent (PolyPlus, NY) according to the manufacturer's instructions. For fluorescent fructose studies, 1-NBDF was used at 10 μM concentration and incubated for 1 hour in complete cell culture media without glucose. Fluorescence was visualized using EVOS FL Auto 2 (Life Technologies, CA) with GFP light cubes (470/22-nm excitation; 510/42-nm emission). Colonic organoids were generated from induced pluripotent stem cells as previously described (*21*), fixed, and embedded in paraffin before IHC.

KHK stable overexpression

The pCDH-EF1α-MCS-T2A-RFP-Puro plasmid (Systems Biosciences, catalog no. CD822A-1) was used to produce lentivirus expressing exogenous KHK. Cells were cultured to 70% confluence for lentiviral transfection. Culture medium with varying viral titers an polybrene (4 μg/ml; Sigma-Aldrich, catalog no. TR1003) was added, and cells were immediately spun at 2200 rpm for 1 hour at room temperature and then transferred to an incubator for 24 hours. Viral titer was then removed, and cells were washed with phosphate-buffered saline (PBS) and incubated in standard culture media for 1 day. Stable transfectants were selected by incubating with puromycin dihydrochloride (2 μg/ml; Sigma-Aldrich, catalog no. P9620) for 3 days and then expanded for 2 to 3 weeks in standard culture media. Cells were then sorted and collected on the basis of red fluorescent protein (RFP) expression using a FACSAria Flow Cytometer (BD Biosciences).

Cell lysis and Western blotting

Cells were lysed in Pierce RIPA buffer with 100 Halt protease and phosphatase inhibitor cocktail (Thermo Fisher Scientific). The samples were resolved by 4 to 12% SDS–polyacrylamide gel electrophoresis and transferred to nitrocellulose membranes. The blots were blocked with 5% bovine serum albumin and 1% Tween 20 tris-buffered saline. Primary antibody concentrations were used according to the manufacturer's recommendations.

Histology and IHC of murine models and human tissues

All normal mouse tissues were obtained from the C57/BL6 background. Harvested tissues were fixed in 10% neutral-buffered formalin and embedded in paraffin before sectioning. Human liver FFPE sections were obtained from patients who underwent liver biopsies or resection at Memorial Sloan Kettering Cancer Center from 2007 to 2017 as part of the management of their benign or neoplastic liver lesions. All human work was approved by the Memorial Sloan Kettering (MSK) Institutional Review Board under protocol #06-107, and informed consent is acquired from patients before biopsy. The median age of the patients included in this study was 55.5 years (range, 22 to 83). The IHC detection of KHK was performed at the Molecular Cytology Core Facility of Memorial Sloan Kettering Cancer Center, using a Discovery XT processor (Ventana Medical Systems). Slides were counterstained with hematoxylin and coverslipped with Permount (Thermo Fisher Scientific). A rabbit monoclonal HNF4α antibody (Cell Signaling Technology, catalog no. 3113) was used in 0.1 μg/ml concentration. The incubation with the primary antibody was done for 5 hours, followed by 60 min of incubation with biotinylated goat anti-rabbit immunoglobulin G (IgG) (Vector Laboratories, catalog no. PK6101) in blocker D (5.75 μg/ml) and streptavidin–horseradish peroxidase, and a DAB detection kit (Ventana Medical Systems) was used according to the manufacturer's instructions. A rabbit monoclonal KHK (Sigma-Aldrich, catalog no. HPA007040) was used in 5 μg/ml concentration. The pathologist (C.S.) reviewed the hematoxylin and eosin stain and IHC-stained slides blinded to patient identification and prior diagnosis. The percentage of positive staining cells and intensity of staining were recorded to calculate an *H*-score.

Of the 27 sections reviewed by the pathologist, eight slides were identified as HCC, seven were identified as hepatocellular adenoma, three were identified as steatotic, and nine were identified as benign.

TCGA bioinformatics analysis

The expression of *SLC2A2*, *KHK*, and *ALDOB* was quantified using the liver hepatocellular carcinoma (LIHC) dataset from the TCGA. This dataset consisted of a total of 369 tumor and 50 normal samples. The expression level was expressed as $\log_2$(TPM + 1) with a $\log_2$(FC) cutoff = 1, *P* value cutoff = 0.05, and a jitter size = 0.4. Clustering of LIHC based on integrative molecular subtyping was performed on the basis of previously defined sequencing performed by the TCGA (*10*). KHK expression data for all other TCGA cancer types were quantified with the same parameters described above. All analyses were performed on the Gene Expression Profiling Interactive Analysis (*38*) interface developed by Peking University, Beijing, China (http://gepia2.cancer-pku.cn/#index).

Metabolite identification using nuclear magnetic resonance

Extracellular metabolites in cell culture media were directly measured using 1H nuclear magnetic resonance (NMR) on a 14.1-T NMR spectrometer (Bruker Biospin), after addition of 100 ml of 10 mM PBS in D_2O, containing 0.5 mM dextran sulfate sodium as an internal standard and 10 mM imidazole as a pH indicator to 100 ml of media. Cell culture and tissue metabolites were extracted with addition of 80% ice-cold methanol. Extracts were placed at 80°C overnight and then centrifuged, and the supernatant was isolated and lyophilized. The dried water-soluble extract was dissolved in 600 ml of standard and 10 mM imidazole as pH indicator. NMR spectroscopy was performed on a 14.1-T NMR spectrometer (Bruker Biospin), equipped with a cryoprobe and automatic sample changer. 1H and 13C spectra were acquired, and resonances were quantified using Chenomx NMR Suite (Chenomx Inc.).

LC-MS metabolomics

Cells were incubated with [U-$^{13}C_6$]fructose for 4 hours, washed twice with ice-cold PBS, and lysed with 80% methanol (in water). Targeted LC-MS analyses were conducted on a Q Exactive Orbitrap Mass Spectrometer (Thermo Fisher Scientific) coupled to a Vanquish UPLC (ultra-performance liquid chromatography) system (Thermo Fisher Scientific), and the mass spectrometer was operated in polarity-switching mode. A SeQuant ZIC-HILIC column (2.1 mm i.d. by 150 mm, Merck) was used for separation of metabolites, and the flow rate was 150 ml/min. Buffers consisted of 100% acetonitrile for A and 0.1% ammonium hydroxide/20 mM ammonium acetate in water for B. Gradient ran from 30% A for 20 min, followed by a wash with 30% A and re-equilibration at 85% A. Metabolites and their ^{13}C isotopologs were identified on the basis of standard retention time and exact mass within 5 ppm. The relative quantification was performed on the basis of the metabolite peak area. All data analyses were performed using in-house written scripts.

Mouse models

Autochthonous liver cancer model with SV40 large T antigen as a defined tumor-specific oncogenic driver antigen (AST cancer model)

Cre/loxP-based cancer mouse models allow tumors to form within their physiologic environment in a temporally and spatially controlled manner. Albumin-floxstop-Tag (AST) mice contain a loxP-flanked stop cassette followed by the oncogenic SV40 large T antigen (Tag) under the control of the albumin-promoter/enhancer sequence to limit the expression of Tag to hepatocytes (*39*, *40*). Tag initiates tumor formation by inhibiting tumor suppressors, including p53 and Rb family members, and is also a potent antigen target for CD8 T cells (*41*). Cre recombinase excises the stop cassette, initiating Tag expression. Cre recombination can be mediated, and tumors were initiated as follows: ASTxAlb:Cre AST mice are crossed to Alb:Cre [Alb:Cre (B6.Cg-Tg(Alb-cre)21Mgn/J)] mice (Jackson Laboratories), which constitutively express Cre recombinase in hepatocytes. In ASTxAlb:Cre mice, Cre recombinase leads to the excision of the stop cassette neonatally and results in SV40 Tag oncogene expression and subsequent tumor initiation in hepatocytes after birth.

The tamoxifen-induced liver cancer model (ASTxCre-ER^{T2})

These mice are generated by crossing the same AST mice with Cre-ER^{T2} [B6.129-Gt(ROSA)26Sor$^{tm1(cre/ERT2)Tyj}$/J] mice (Jackson Laboratories) to generate mice where hepatocellular tumorigenesis is initiated by tamoxifen administration (*42*). All other GEM models of liver cancer were developed by the Lowe laboratory as previously described (*43*). All animal experiments were approved by the Institutional Animal Care and Use Committee at Memorial Sloan Kettering Cancer Center.

Mouse infusion studies and NMR analysis

Five hundred microliters of fructose (4000 mg/kg) was intraperitoneally injected to each mouse. After 5 min, the mouse was kept under isoflurane for 1 min, and 200 μl of blood sample was collected in microtainer tubes (BD-365985) via a retro-orbital procedure. After cervical dislocation, liver samples were collected (~8 min from intraperitoneal injection) and quickly snap-frozen. Blood samples were centrifuged at 14,000 rpm for 10 min. Fifty microliters of plasma was added to 650 μl of standard containing 100 mM sodium phosphate (90% H_2O and 10% D_2O), 1 mM methionine ($^{13}CH_3$) as a concentration reference standard, the final pH adjusted to 6.6 and placed into a 5-mm NMR tube for subsequent NMR analysis. For each liver, stratified random sampling (three to five regions) has been done to find representative properties associated with the entire liver. A mass of 200 mg of wet weight of liver was dissected. A solution of perchloric acid (4%; 1:4, w/v) was added to pooled tumors from each mouse inside the prefilled bead mill tubes (Thermo Fisher Scientific, catalog no. 15-340-151). The tissues were finely grounded in Bead Ruptor 24 Bead Mill Homogenizer (Omni international Inc.) for 3 min. Next, the vials were centrifuged at 14,000 rpm for 15 min. The supernatant was transferred to a new 5-ml Eppendorf tube, where chloroform/tri-*n*-octylamine (78%/22%, v/v) was added in a 1:2 volumetric ratio. The samples were centrifuged at 4000 rpm for 15 min; the aqueous phase was removed and transferred to a 20-ml scintillation glass vial and then lyophilized. Then, dried samples were dissolved in 700 μl of standard containing 100 mM sodium phosphate (90% H_2O and 10% D_2O), 1 mM methionine ($^{13}CH_3$) as a concentration reference standard, the final pH adjusted to 6.6 and placed into a 5-mm NMR tube for subsequent NMR analysis. NMR acquisition was performed on a 14.1-T NMR spectrometer equipped with an auto sampler and ^{13}C probe (Bruker Biospin). 1D^{13}C NMR spectra for each sample were acquired with a delay of 2 s, acquisition time of 1.27 s, 30° pulse, and 1024 averages. Resonances of each metabolite were identified using commercial standard solution made in our laboratory, and bar plots were generated using GraphPad Prism software.

Synthesis of deuterated [2-^{13}C]-D-fructose 3

A total of 2.0 g of [2-^{13}C]-D-fructose (10.75 mmol) and 100 ml of HPLC grade methanol were added to a 250-ml Erlenmeyer flask. Once dissolved, 100 μl of acetyl chloride (110.4 mg, 1.406 mmol, 0.15 equiv) was added, and the reaction mixture was sealed and stirred at room temperature overnight. Amberlite IRA-410 OH resin (2 g) was then added and stirred for 15 min. The reaction mixture was filtered and the resin was washed twice with 50 ml of methanol. The solvent was evaporated to afford **1** as a clear oil. The oil was used directly in the next reaction as is. The deuteration of **1** was adopted from previously reported methods (*44*). A total of 21.3 ml of D_2O (0.25 M) was added to 100-ml round bottom flask containing 1.04 g of **1** (5.33 mmol). Freshly ground NaOH (85 mg; 2.13 mmol, 0.4 equiv) was added to the reaction mixture. Ru/C (2.1 g of 5 wt %) was added to the reaction mixture. H_2 was bubbled into the reaction mixture for 15 min. The reaction mixture was then stirred under H_2 at 80°C. After 24 hours, the reaction mixture was filtered and washed with 100 ml of H_2O. The reaction mixture was brought up to pH 7 by addition of DOWEX 50WX8 hydrogen form resin. The resin was filtered and the solution was lyophilized to afford a clear oil. This procedure was repeated twice until deuterium incorporation of **2** was found by NMR to be >96%. A total of 3.9 ml of 0.001 M HCl in H_2O was added to 367 mg of **2** (1.96 mmol). The reaction mixture was refluxed with a Dean-Stark trap for 3 hours (water in the Dean-Stark trap). After 3 hours, the reaction mixture was cooled and IRA-410 OH resin was added to pH 7. The reaction mixture was filtered and lyophilized to give a clear foam. The product was purified by reverse-phase HPLC to give **3** as a solid upon evaporation.

Hyperpolarized fructose magnetic resonance and T_1 measurements at 1 T

Dynamic nuclear polarization was performed with a 5.0-T SpinLab Hyperpolarizer (GE Healthcare). A 2.0 M solution of **3** dissolved in water containing 15 mM OX063 trityl radical (Oxford Instruments) was polarized in a 5.0-T SpinLab Hyperpolarizer for 3 hours. The hyperpolarized substrate was ejected from the polarizer via dissolution with a large excess of superheated D_2O to a final concentration of 25 mM with a resultant pH of 7.2. Polarization quantification was carried immediately after dissolution. One milliliter of the hyperpolarized dissolution was added to an NMR tube and transferred to a 1-T Spinsolve ^{13}C NMR spectrometer (Magritek, NZ). NMR spectra were acquired every 3 s with a 5° excitation over 3 min. Apparent relaxation time (T_1) was fitted to a mono-exponential curve and corrected for flip angle. Thermal polarization was determined from the average spectrum of 1024 scans acquired with 90° flip angle every 10 s. Final polarization values after correcting for flip angles and the apparent T_1 were calculated to be 5 to 10% for all HP fructose dissolutions. Substrate concentration was measured by ^{13}C NMR at 14.1 T in the presence of 1 mM Gd-DOTA and 15 mM [^{13}C]-acetate standard. The integral of the C_2 carbon of fructose was compared to that of the acetate standard to calculate concentrations.

Hyperpolarized fructose magnetic resonance imaging

All animal experiments were approved by the Institutional Animal Care and Use Committee at Memorial Sloan Kettering Cancer Center (protocol number 13-12-019). A 1/3 mm diameter, 28-cm-long catheter (Braintree Scientific, USA) was placed in the lateral tail vein of mice (8 to 9 weeks old), and a heparing (10 U/ml) in saline solution was used to prevent coagulation and blockage of the catheter. The mouse was anesthetized with 1 liter/min room air and 1.5% isoflurane and loaded in a Bruker 3 T magnetic resonance imaging (MRI) equipped with a dual tune ^{1}H/^{13}C coil. A 4 M [^{13}C, ^{15}N]-acetonitrile phantom was placed beside the mouse, and the mouse was positioned such that its liver was centered within the coil. Axial ^{1}H-T_2-weighted spin echo images were acquired before MRSI (magnetic resonance spectroscopy imaging) studies to denote anatomy and place voxels on the region of interest using 36 mm by 30 mm field of view (FOV), 10 slices at 2 mm per slice. Intravenous injection of HP **3** in D_2O was started 20 s after dissolution. HP solution (250 μl) was injected over 10 s via the implanted tail catheter. An axial two-dimensional (2D) CSI (chemical shift imagery) sequence was used to acquire HP fructose MRS. 2D CSI data were acquired immediately after the injection was completed for 20 s with 20° constant flip angle, 6.75 mm × 5.625 mm resolution, 36 mm by 30 mm FOV, 10-mm slab thickness, 8 by 8 image size, and 1.67 Hz per points spectral resolution.

Image reconstruction

Data were reconstructed offline using MATLAB (MathWorks). The data were zero-filled in the spectral and spatial dimensions to 256 spectral points and 16 × 16 spatial points and baseline-corrected. Only voxels containing >80% liver by voxel volume were chosen for quantification and statistical analysis to limit the influence of partial volume effects and metabolism in adjacent tissue.

HP MRI analysis

For animal studies, $n = 3$ or $n = 4$ was selected to validate the HP biomarker procedure. No samples or animals were excluded from data analyses. Quantification of NMR spectra obtained after reconstruction was performed using Mnova NMR. The peak area of the pyranose isoform of HP [2-^{13}C]-fructose (98 ppm) and HP [2-^{13}C] fructose-1-phosphate (99 ppm) and the furanose isoform of HP [2-^{13}C]-fructose (102 ppm) were used to calculate relevant ratios. The ratio of furanose isoform of HP [2-^{13}C]fructose to total carbon was expressed using the following formula: furanose isoform of HP [2-^{13}C]fructose/pyranose isoform of HP [2-^{13}C]fructose + HP [2-^{13}C]fructose-1-phosphate + furanose isoform of HP [2-^{13}C]fructose). Fructose to fructose-1-phophate was used to calculate relevant ratios. Quantitative data are representative of means ± SD and determined to be statistically significant when $P < 0.05$ by two-tailed Student's t test. In figures, asterisks denote statistical significance as calculated by Student's t test (*$P < 0.05$; **$P < 0.01$; ***$P < 0.001$; ****$P < 0.0001$).

Statistical analysis

A two-tailed, unpaired Student's t test was used to calculate P values, with $P < 0.05$ used to determine statistical significance.

SUPPLEMENTARY MATERIALS

Supplementary material for this article is available at https://science.org/doi/10.1126/sciadv.abm7985

View/request a protocol for this paper from *Bio-protocol*.

REFERENCES AND NOTES

1. M. Dashty, A quick look at biochemistry: Carbohydrate metabolism. *Clin. Biochem.* **46**, 1339–1352 (2013).
2. M. L. Cardenas, A. Cornish-Bowden, T. Ureta, Evolution and regulatory role of the hexokinases. *Biochim. Biophys. Acta* **1401**, 242–264 (1998).
3. G. T. Cori, S. Ochoa, M. W. Slein, C. F. Cori, The metabolism of fructose in liver; isolation of fructose-l-phosphate and inorganic pyrophosphate. *Biochim. Biophys. Acta* **7**, 304–317 (1951).

4. V. Douard, R. P. Ferraris, Regulation of the fructose transporter GLUT5 in health and disease. *Am. J. Physiol. Endocrinol. Metab.* **295**, E227–E237 (2008).
5. M. Ali, P. Rellos, T. M. Cox, Hereditary fructose intolerance. *J. Med. Genet.* **35**, 353–365 (1998).
6. B. E. Hayward, D. T. Bonthron, Structure and alternative splicing of the ketohexokinase gene. *Eur. J. Biochem.* **257**, 85–91 (1998).
7. X. Li, X. Qian, L. X. Peng, Y. Jiang, D. H. Hawke, Y. Zheng, Y. Xia, J. H. Lee, G. Cote, H. Wang, L. Wang, C. N. Qian, Z. Lu, A splicing switch from ketohexokinase-C to ketohexokinase-A drives hepatocellular carcinoma formation. *Nat. Cell Biol.* **18**, 561–571 (2016).
8. M. A. Lanaspa, L. G. Sanchez-Lozada, C. Cicerchi, N. Li, C. A. Roncal-Jimenez, T. Ishimoto, M. le, G. E. Garcia, J. B. Thomas, C. J. Rivard, A. Andres-Hernando, B. Hunter, G. Schreiner, B. Rodriguez-Iturbe, Y. Y. Sautin, R. J. Johnson, Uric acid stimulates fructokinase and accelerates fructose metabolism in the development of fatty liver. *PLoS One* **7**, e47948 (2012).
9. J. S. Hwa, H. J. Kim, B. M. Goo, H. J. Park, C. W. Kim, K. H. Chung, H. C. Park, S. H. Chang, Y. W. Kim, D. R. Kim, G. J. Cho, W. S. Choi, K. R. Kang, The expression of ketohexokinase is diminished in human clear cell type of renal cell carcinoma. *Proteomics* **6**, 1077–1084 (2006).
10. D. A. Wheeler, L. R. Roberts; Cancer Genome Atlas Research Network. Electronic address, N. Cancer Genome Atlas Research, Comprehensive and Integrative Genomic Characterization of Hepatocellular Carcinoma. *Cell* **169**, 1327–1341.e1323 (2017).
11. C. A. Lyssiotis, L. C. Cantley, F stands for fructose and fat. *Nature* **502**, 181–182 (2013).
12. S. S. Tee, K. R. Keshari, Novel approaches to imaging tumor metabolism. *Cancer J.* **21**, 165–173 (2015).
13. J. H. Ardenkjaer-Larsen, B. Fridlund, A. Gram, G. Hansson, L. Hansson, M. H. Lerche, R. Servin, M. Thaning, K. Golman, Increase in signal-to-noise ratio of & >10,000 times in liquid-state NMR. *Proc. Natl. Acad. Sci. U.S.A.* **100**, 10158–10163 (2003).
14. S. J. Nelson, J. Kurhanewicz, D. B. Vigneron, P. E. Z. Larson, A. L. Harzstark, M. Ferrone, M. van Criekinge, J. W. Chang, R. Bok, I. Park, G. Reed, L. Carvajal, E. J. Small, P. Munster, V. K. Weinberg, J. H. Ardenkjaer-Larsen, A. P. Chen, R. E. Hurd, L.-I. Odegardstuen, F. J. Robb, J. Tropp, J. A. Murray, Metabolic imaging of patients with prostate cancer using hyperpolarized [1-(1)(3)C]pyruvate. *Sci. Transl. Med.* **5**, 198ra108 (2013).
15. C. H. Cunningham, J. Y. C. Lau, A. P. Chen, B. J. Geraghty, W. J. Perks, I. Roifman, G. A. Wright, K. A. Connelly, Hyperpolarized 13C metabolic MRI of the human heart: Initial experience. *Circ. Res.* **119**, 1177–1182 (2016).
16. V. Z. Miloushev, K. L. Granlund, R. Boltyanskiy, S. K. Lyashchenko, L. M. DeAngelis, I. K. Mellinghoff, C. W. Brennan, V. Tabar, T. J. Yang, A. I. Holodny, R. E. Sosa, Y. W. W. Guo, A. P. Chen, J. Tropp, F. Robb, K. R. Keshari, Metabolic Imaging of the human brain with hyperpolarized ^{13}C Pyruvate demonstrates ^{13}C lactate production in brain tumor patients. *Cancer Res.* **78**, 3755–3760 (2018).
17. K. R. Keshari, D. M. Wilson, A. P. Chen, R. Bok, P. E. Z. Larson, S. Hu, M. V. Criekinge, J. M. Macdonald, D. B. Vigneron, J. Kurhanewicz, Hyperpolarized [2-13C]-fructose: A hemiketal DNP substrate for in vivo metabolic imaging. *J. Am. Chem. Soc.* **131**, 17591–17596 (2009).
18. C. P. Diggle, M. Shires, D. Leitch, D. Brooke, I. M. Carr, A. F. Markham, B. E. Hayward, A. Asipu, D. T. Bonthron, Ketohexokinase: Expression and localization of the principal fructose-metabolizing enzyme. *J. Histochem. Cytochem.* **57**, 763–774 (2009).
19. R. C. Adelman, F. J. Ballard, S. Weinhouse, Purification and properties of rat liver fructokinase. *J. Biol. Chem.* **242**, 3360–3365 (1967).
20. M. Gordillo, T. Evans, V. Gouon-Evans, Orchestrating liver development. *Development* **142**, 2094–2108 (2015).
21. M. Crespo, E. Vilar, S. Y. Tsai, K. Chang, S. Amin, T. Srinivasan, T. Zhang, N. H. Pipalia, H. J. Chen, M. Witherspoon, M. Gordillo, J. Z. Xiang, F. R. Maxfield, S. Lipkin, T. Evans, S. Chen, Colonic organoids derived from human induced pluripotent stem cells for modeling colorectal cancer and drug testing. *Nat. Med.* **23**, 878–884 (2017).
22. N. Fedchenko, J. Reifenrath, Different approaches for interpretation and reporting of immunohistochemistry analysis results in the bone tissue - A review. *Diagn. Pathol.* **9**, 221 (2014).
23. A. Cho, R. Eskandari, V. Z. Miloushev, K. R. Keshari, A non-synthetic approach to extending the lifetime of hyperpolarized molecules using D2O solvation. *J. Magn. Reson.* **295**, 57–62 (2018).
24. Y. Sawama, Y. Yabe, H. Iwata, Y. Fujiwara, Y. Monguchi, H. Sajiki, Stereo- and regioselective direct multi-deuterium-labeling methods for sugars. *Chemistry* **18**, 16436–16442 (2012).
25. N. Springer, S. Lindbloom-Hawley, T. Schermerhorn, Tissue expression of ketohexokinase in cats. *Res. Vet. Sci.* **87**, 115–117 (2009).
26. A. Flamholz, E. Noor, A. Bar-Even, W. Liebermeister, R. Milo, Glycolytic strategy as a tradeoff between energy yield and protein cost. *Proc. Natl. Acad. Sci. U.S.A.* **110**, 10039–10044 (2013).
27. R. D. Feinman, E. J. Fine, Fructose in perspective. *Nutr Metab (Lond)* **10**, 45 (2013).
28. S. Z. Sun, M. W. Empie, Fructose metabolism in humans - what isotopic tracer studies tell us. *Nutr Metab (Lond)* **9**, 89 (2012).
29. M. D. Goncalves, C. Lu, J. Tutnauer, T. E. Hartman, S. K. Hwang, C. J. Murphy, C. Pauli, R. Morris, S. Taylor, K. Bosch, S. Yang, Y. Wang, J. van Riper, H. C. Lekaye, J. Roper, Y. Kim, Q. Chen, S. S. Gross, K. Y. Rhee, L. C. Cantley, J. Yun, High-fructose corn syrup enhances intestinal tumor growth in mice. *Science* **363**, 1345–1349 (2019).
30. A. Asipu, B. E. Hayward, J. O'Reilly, D. T. Bonthron, Properties of normal and mutant recombinant human ketohexokinases and implications for the pathogenesis of essential fructosuria. *Diabetes* **52**, 2426–2432 (2003).
31. K. Kishida, S. C. Pearce, S. Yu, N. Gao, R. P. Ferraris, Nutrient sensing by absorptive and secretory progenies of small intestinal stem cells. *Am. J. Physiol. Gastrointest. Liver Physiol.* **312**, G592–G605 (2017).
32. W. L. Chen, Y. Y. Wang, A. Zhao, L. Xia, G. Xie, M. Su, L. Zhao, J. Liu, C. Qu, R. Wei, C. Rajani, Y. Ni, Z. Cheng, Z. Chen, S. J. Chen, W. Jia, Enhanced fructose utilization mediated by SLC2A5 is a unique metabolic feature of acute myeloid leukemia with therapeutic potential. *Cancer Cell* **30**, 779–791 (2016).
33. Y. Weng, X. Fan, Y. Bai, S. Wang, H. Huang, H. Yang, J. Zhu, F. Zhang, SLC2A5 promotes lung adenocarcinoma cell growth and metastasis by enhancing fructose utilization. *Cell Death Discov* **4**, 38 (2018).
34. J. Levi, Z. Cheng, O. Gheysens, M. Patel, C. T. Chan, Y. Wang, M. Namavari, S. S. Gambhir, Fluorescent fructose derivatives for imaging breast cancer cells. *Bioconjug. Chem.* **18**, 628–634 (2007).
35. M. Wuest, B. J. Trayner, T. N. Grant, H. S. Jans, J. R. Mercer, D. Murray, F. G. West, A. J. B. McEwan, F. Wuest, C. I. Cheeseman, Radiopharmacological evaluation of 6-deoxy-6-[18F]fluoro-D-fructose as a radiotracer for PET imaging of GLUT5 in breast cancer. *Nucl. Med. Biol.* **38**, 461–475 (2011).
36. A. Andres-Hernando, D. J. Orlicky, M. Kuwabara, T. Ishimoto, T. Nakagawa, R. J. Johnson, M. A. Lanaspa, Deletion of fructokinase in the liver or in the intestine reveals differential effects on sugar-induced metabolic dysfunction. *Cell Metab.* **32**, 117–127.e113 (2020).
37. C. Jang, S. Wada, S. Yang, B. Gosis, X. Zeng, Z. Zhang, Y. Shen, G. Lee, Z. Arany, J. D. Rabinowitz, The small intestine shields the liver from fructose-induced steatosis. *Nat. Metab.* **2**, 586–593 (2020).
38. Z. Tang, C. Li, B. Kang, G. Gao, C. Li, Z. Zhang, GEPIA: A web server for cancer and normal gene expression profiling and interactive analyses. *Nucleic Acids Res.* **45**, W98–W102 (2017).
39. A. Schietinger, J. J. Delrow, R. S. Basom, J. N. Blattman, P. D. Greenberg, Rescued tolerant CD8 T cells are preprogrammed to reestablish the tolerant state. *Science* **335**, 723–727 (2012).
40. M. Philip, L. Fairchild, L. Sun, E. L. Horste, S. Camara, M. Shakiba, A. C. Scott, A. Viale, P. Lauer, T. Merghoub, M. D. Hellmann, J. D. Wolchok, C. S. Leslie, A. Schietinger, Chromatin states define tumour-specific T cell dysfunction and reprogramming. *Nature* **545**, 452–456 (2017).
41. S. Stahl, T. Sacher, A. Bechtold, U. Protzer, R. Ganss, G. J. Hämmerling, B. Arnold, N. Garbi, Tumor agonist peptides break tolerance and elicit effective CTL responses in an inducible mouse model of hepatocellular carcinoma. *Immunol. Lett.* **123**, 31–37 (2009).
42. A. Schietinger, M. Philip, V. E. Krisnawan, E. Y. Chiu, J. J. Delrow, R. S. Basom, P. Lauer, D. G. Brockstedt, S. E. Knoblaugh, G. J. Hämmerling, T. D. Schell, N. Garbi, P. D. Greenberg, Tumor-specific T cell dysfunction is a dynamic antigen-driven differentiation program initiated early during tumorigenesis. *Immunity* **45**, 389–401 (2016).
43. E. R. Kastenhuber, G. Lalazar, S. L. Houlihan, D. F. Tschaharganeh, T. Baslan, C. C. Chen, D. Requena, S. Tian, B. Bosbach, J. E. Wilkinson, S. M. Simon, S. W. Lowe, DNAJB1–PRKACA fusion kinase interacts with β-catenin and the liver regenerative response to drive fibrolamellar hepatocellular carcinoma. *Proc. Natl. Acad. Sci. U.S.A.* **114**, 13076–13084 (2017).
44. C. Taglang, D. E. Korenchan, C. von Morze, J. Yu, C. Najac, S. Wang, J. E. Blecha, S. Subramaniam, R. Bok, H. F. Van Brocklin, D. B. Vigneron, S. M. Ronen, R. Sriram, J. Kurhanewicz, D. M. Wilson, R. R. Flavell, Late-stage deuteration of 13C-enriched substrates for T1 prolongation in hyperpolarized 13C MRI. *Chem. Commun. (Camb.)* **54**, 5233–5236 (2018).

Acknowledgments

Funding: This work was supported, in part, by U.S. NIH grants R21CA212958 (K.R.K.), R01CA237466 (K.R.K.), R01CA252037 (K.R.K.), and K99CA226357 (S.J.); by Cancer Center Support Grant P30CA008748 (K.R.K. and C.B.T.); and by grants from the Center for Molecular Imaging and Nanotechnology at Memorial Sloan Kettering Cancer Center (K.R.K.), Tow Foundation (R.E.), Emerson Collective (K.R.K.), the Thompson Family Foundation (K.R.K.), and the Ludwig Center for Basic and Translational Immunology (K.R.K.). **Author contributions:** S.S.T., N.K., Q.C., R.E., C.B.T., and K.R.K. designed the study and experiments. S.S.T., N.K., Q.C., R.E., A.M., R.M.S., R.C., S.J., M.S., E.R.K., S.C., C.S., S.W. L., A.S., and W.R.J., performed experiments and provided samples. S.S.T., N.K., Q.C., R.E., C.B.T., and K.R.K. analyzed the data. S.S.T., N.K., Q.C., R.E., C.B.T., and K.R.K. wrote the manuscript. **Competing interests:** C.B.T. is a founder of

Agios Pharmaceuticals and a member of its scientific advisory board. He is also a former member of the Board of Directors and stockholder of Merck and Charles River Laboratories. He is a named inventor on patents related to cellular metabolism. These patents are not directly related to the studies in this manuscript. K.R.K. serves on the scientific advisory board of NVision Imaging Technologies. He is a named inventor on patents related to imaging of cellular metabolism that are not related to this work. He is also named as an inventor on a patent that details the use of hyperpolarized fructose (WO2011029854A1) as well as a recent patent submission (U.S. patent application number 16/646549) related to the use of deuterated solvents in hyperpolarized MRI. All other authors declare that they have no competing interests. **Data and materials availability:** All data needed to evaluate the conclusions in the paper are present in the paper and/or the Supplementary Materials.

Submitted 14 October 2021
Accepted 15 February 2022
Published 6 April 2022
10.1126/sciadv.abm7985